

1 **Functional genomic screens identify human host factors for SARS-CoV-2 and**
2 **common cold coronaviruses**

3

4 Ruofan Wang^{1,*}, Camille R. Simoneau^{2,*}, Jessie Kulsuptrakul¹, Mehdi Bouhaddou^{2,3,4},
5 Katherine Travisano¹, Jennifer M. Hayashi², Jared Carlson-Stevermer⁵, Jennifer Oki⁵,
6 Kevin Holden⁵, Nevan J. Krogan^{2,3,4}, Melanie Ott², Andreas S. Puschnik^{1,#}

7

8 ¹ Chan Zuckerberg Biohub, San Francisco, CA, 94158, USA

9 ² Gladstone Institutes, San Francisco, CA 94158, USA

10 ³ University of California San Francisco, Quantitative Biosciences Institute (QBI), San
11 Francisco, CA, 94158, USA

12 ⁴ University of California San Francisco, Department of Cellular and Molecular
13 Pharmacology, San Francisco, CA, 94158, USA

14 ⁵ Synthego Corporation, Menlo Park, CA 94025

15 * These authors contributed equally to this work

16 # Corresponding author: andreas.puschnik@czbiohub.org

17

18 **Abstract**

19 The *Coronaviridae* are a family of viruses that causes disease in humans ranging from
20 mild respiratory infection to potentially lethal acute respiratory distress syndrome. Finding
21 host factors that are common to multiple coronaviruses could facilitate the development
22 of therapies to combat current and future coronavirus pandemics. Here, we conducted
23 parallel genome-wide CRISPR screens in cells infected by SARS-CoV-2 as well as two

24 seasonally circulating common cold coronaviruses, OC43 and 229E. This approach
25 correctly identified the distinct viral entry factors ACE2 (for SARS-CoV-2),
26 aminopeptidase N (for 229E) and glycosaminoglycans (for OC43). Additionally, we
27 discovered phosphatidylinositol phosphate biosynthesis and cholesterol homeostasis as
28 critical host pathways supporting infection by all three coronaviruses. By contrast, the
29 lysosomal protein TMEM106B appeared unique to SARS-CoV-2 infection.
30 Pharmacological inhibition of phosphatidylinositol phosphate biosynthesis and
31 cholesterol homeostasis reduced replication of all three coronaviruses. These findings
32 offer important insights for the understanding of the coronavirus life cycle as well as the
33 potential development of host-directed therapies.

34

35 **Introduction**

36 The *Coronaviridae* family includes seven known human pathogens, for which there are
37 no approved vaccines and only limited therapeutic options. The seasonally circulating
38 human coronaviruses (HCoV) OC43, HKU1, 229E and NL63 cause mild, common cold-
39 like, respiratory infections in humans ¹. However, three highly pathogenic coronaviruses
40 emerged in the last two decades, highlighting the pandemic potential of this viral family ²⁻
41 ⁴. Infection with severe acute respiratory syndrome coronavirus 1 (SARS-CoV-1) and
42 Middle East respiratory syndrome coronavirus (MERS-CoV) can lead to acute respiratory
43 distress syndrome and death, with fatality rates between 10-40% ⁵. SARS-CoV-2, which
44 is currently causing a global pandemic, is less deadly but far more transmissible than
45 SARS-CoV-1 and MERS-CoV, and has been responsible for over 32 million cases and
46 900,000 deaths globally so far ^{5,6}. Because of the severity of their impact on global health,

47 it is critical to understand how SARS-CoV-2 and other coronaviruses hijack the host cell
48 machinery during infection, and apply this knowledge to develop new therapeutic
49 strategies.

50

51 Coronaviruses are enveloped, positive-sense, single-stranded RNA viruses with a
52 genome length of approximately 30kb. Upon receptor binding and membrane fusion, the
53 viral RNA is released into the cytoplasm, where it is translated to produce viral proteins.
54 Subsequently, the viral replication/transcription complexes form on double-membrane
55 vesicles and generate genome copies. These are then packaged into new virions via a
56 budding process, through which they acquire the viral envelope, and the resulting virions
57 are released from infected cells ⁷. During these steps, specific cellular proteins are
58 hijacked and play crucial roles in the viral life cycle. For example, the angiotensin-
59 converting enzyme 2 (ACE2) is exploited as the viral entry receptor for HCoV-NL63,
60 SARS-CoV-1 and SARS-CoV-2 ⁸⁻¹⁰. Additionally, cellular proteases, such as TMPRSS2,
61 cathepsin L and furin, are important for the cleavage of the viral spike (S) protein of
62 several coronaviruses, thereby mediating efficient membrane fusion with host cells ¹¹⁻¹⁵.
63 Systematic studies have illuminated virus-host interactions during the later steps of the
64 viral life cycle. For example, proteomics approaches revealed a comprehensive
65 interactome between individual SARS-CoV-2 proteins and cellular proteins ^{16,17}.
66 Additionally, biotin labelling identified candidate host factors based on their proximity to
67 coronavirus replicase complexes ¹⁸. While these studies uncovered physical relationships
68 between viral and cellular proteins, they do not provide immediate information about the
69 importance of these host components for viral replication.

70

71 An orthogonal strategy is to screen for mutations that render host cells resistant to viral
72 infection using CRISPR-based mutagenesis. These screens identify host factors that are
73 functionally required for virus replication and could be targets for host-directed therapies
74 ¹⁹. Several groups have already successfully applied this approach, yet with certain
75 limitations, e.g. the use of Vero green monkey cells instead of a human cell line ²⁰, the
76 use of a small CRISPR library only based on the SARS-CoV-2 protein interactome ²¹, or
77 the use of a SARS-CoV-2 harboring a deletion in the spike S1/S2 site due to cell culture
78 adaptation ²².

79

80 In this study, we have performed a genome-wide CRISPR knockout (KO) screen using
81 wild-type SARS-CoV-2 (USA/WA-1 isolate) in human cells. Importantly, we expanded our
82 functional genomics approach to distantly related *Coronaviridae* in order to probe for
83 commonalities and differences across the family. This strategy can reveal potential pan-
84 coronavirus host factors, thus illuminating targets for antiviral therapy to combat current
85 and potential future outbreaks. We conducted comparative CRISPR screens for SARS-
86 CoV-2 and two seasonally circulating common cold coronaviruses, OC43 and 229E. Our
87 results corroborate previously implicated host pathways, uncover new aspects of virus-
88 host interaction and identify targets for host-directed antiviral treatment.

89

90 **Results**

91 CRISPR knockout screens identify common and virus-specific candidate host factors for 92 coronavirus infection

93 Phenotypic selection of virus-resistant cells in a pooled CRISPR KO screen is based on
94 survival and growth differences of mutant cells upon virus infection. We chose Huh7.5.1
95 hepatoma cells as they were uniquely susceptible to all tested coronaviruses. We readily
96 observed drastic cytopathic effect during OC43 and 229E infection (Extended Data Fig.
97 1a). Huh7.5.1 also supported high levels of SARS-CoV-2 replication but only displayed
98 limited virus-induced cell death (Extended Data Fig. 1b,c). To improve selection
99 conditions for the SARS-CoV-2 CRISPR screen, we overexpressed ACE2 and/or
100 TMPRSS2, which are present at low levels in WT Huh7.5.1 cells (Extended Data Fig. 1d).
101 This led to increased viral uptake of a SARS-CoV-2 spike-pseudotyped lentivirus,
102 confirming the important function of ACE2 and TMPRSS2 for SARS-CoV-2 entry
103 (Extended Data Fig. 1e). We ultimately used Huh7.5.1 cells harboring a bicistronic ACE2-
104 IRES-TMPRSS2 construct for the SARS-CoV-2 screen as these cells sustained efficient
105 infection that led to widespread cell death, while still allowing the survival of a small
106 number of cells (Extended Data Fig. 1c).

107

108 The three CRISPR screens - for resistance to SARS-CoV-2, HCoV-229E and HCoV-
109 OC43 - identified a compendium of critical host factors across the human genome (Fig.
110 1a, Supplementary Table 1). Importantly, the known viral entry receptors ranked among
111 the top hits: ACE2 for SARS-CoV-2 and aminopeptidase N (ANPEP) for 229E (Fig. 1b,c)
112 ^{8,23}. OC43, unlike the other coronaviruses, does not have a known proteinaceous receptor

113 but primarily depends on sialic acid or glycosaminoglycans for cell entry ^{24,25}; consistent
114 with this fact, multiple heparan sulfate biosynthetic genes (B3GALT6, B3GAT3,
115 B4GALT7, EXT1, EXT2, EXTL3, FAM20B, NDST1, SLC35B2, UGDH, XYLT2) were
116 identified in our OC43 screen (Fig. 1d, Extended Data Fig. 2a). Several of these genes
117 were also markedly enriched in the SARS-CoV-2 screen, consistent with a recent report
118 that SARS-CoV-2 requires both ACE2 and cellular heparan sulfate for efficient infection
119 (Fig. 1b, Extended Data Fig. 2a) ²⁶. Overall, the identification of the expected entry factors
120 validates the phenotypic selection of our host factor screens.

121
122 Gene Ontology (GO) enrichment analysis found a number of cellular processes to be
123 important for multiple coronaviruses. These included proteoglycan and aminoglycan
124 biosynthesis, vacuolar and lysosomal transport, autophagy, Golgi vesicle transport and
125 phosphatidylinositol metabolic processes (Fig. 2a, Supplementary Table 2).

126 In the phosphatidylinositol metabolic process, the SARS-CoV-2 screen identified VAC14,
127 which is part of the PIKfyve kinase complex (Fig. 1b). PIKFYVE itself was moderately
128 enriched in the SARS-CoV-2 screen (Extended Data Fig. 2a). This complex catalyzes the
129 conversion of phosphatidylinositol-3-phosphate to phosphatidylinositol-3,5-bisphosphate,
130 which is localized to late endosomes ²⁷. Interestingly, the CRISPR screens with HCoV-
131 229E and HCoV-OC43 identified the subunits (PIK3C3, UVRAG, BECN1 and PIK3R4) of
132 the class III phosphatidylinositol 3-kinase (PI3K) complex, which generates the precursor
133 phosphatidylinositol-3-phosphate in early endosome membranes (Fig. 1c,d and Extended
134 Data Fig. 2a) ²⁸. Taken together, our data highlight different steps of the
135 phosphatidylinositol biosynthetic pathway, which regulates endocytic sorting,

136 endomembrane homeostasis and autophagy, to be critical for the life cycle of all three
137 and possibly all coronaviruses.

138

139 Another group of genes found in all three CRISPR screens are linked to cholesterol
140 metabolism. The SARS-CoV-2 resistant cell population contained multiple knockouts in
141 genes of the sterol regulatory element-binding protein (SREBP) pathway (SCAP,
142 MBTPS1, MBTPS2) (Fig. 1b, Extended Data Fig. 2a)²⁹. SCAP is an escort protein for the
143 transport of the transcription factors SREBF1 and SREBF2 from the ER to the Golgi in
144 response to low levels of cholesterol. In the Golgi, the SREBF proteins are sequentially
145 cleaved by the proteases MBTPS1 and MBTPS2. Subsequently, the transcription factors
146 translocate to the nucleus to activate fatty acid and cholesterol biosynthesis. SREBF1
147 and SREBF2 themselves did not score in the screen, potentially due to their functional
148 redundancy. LDLR (Low Density Lipoprotein Receptor), important for cholesterol uptake,
149 was also enriched in both the SARS-CoV-2 and the 229E screen, while SCAP was
150 enriched in the OC43 screen (Extended Data Fig. 2a,b). Additionally, NPC1 (Niemann–
151 Pick intracellular cholesterol transporter 1), which facilitates export of cholesterol from the
152 endolysosomal compartment, ranked highly in the 229E screen (Fig. 1c)³⁰. Overall, our
153 data indicates a strong link between intracellular cholesterol levels and infection by all
154 three coronavirus.

155

156 Some genes were found in the OC43 and 229E screens, but not in the SARS-CoV-2
157 screen. For instance, the common cold coronavirus screens showed a strong overlap of
158 genes, which are important for endosome and autophagosome maturation (Fig. 1c,d and

159 Extended Data Fig. 2b). These include the small GTPase Rab7a, components of the
160 HOPS complex (VPS11, VPS16, VPS18, VPS33A), the Ccz1-Mon1 guanosine exchange
161 complex (CCZ1, CCZ1B, C18orf8), the WDR81-WDR91 complex, and other genes
162 related to lysosome and autophagosome function (SPNS1, TOLLIP, TMEM41B,
163 AMBRA1) ³¹⁻³⁷. We also identified cathepsin L (CTSL1) as well as the mannose-6-
164 phosphate receptor (M6PR) and GNPTAB, which are important for proper trafficking of
165 lysosomal enzymes from the trans-Golgi network ^{38,39}. Interestingly, the HOPS complex,
166 cathepsins, GNPTAB and SPNS1 were previously linked to Ebola virus entry, implying
167 similar viral entry strategies ^{39,40}.

168 The absence of endolysosomal factors in the SARS-CoV-2 screen may be explained by
169 the ectopic expression of the cell-surface protease TMPRSS2 in this screen. The
170 cleavage of SARS-CoV-2 spike can occur either at the plasma membrane via TMPRSS2
171 or in endolysosomes through cathepsins. Sufficient TMPRSS2 levels may thus ablate the
172 requirement for cathepsin and other factors linked to endolysosomal activity ¹¹. Consistent
173 with this hypothesis, a CRISPR screen using a SARS-CoV-2 with a spike S1/S2 site
174 deletion, which preferentially uses the endolysosomal entry route, showed strong
175 enrichment in RAB7A, the Ccz1-Mon1 guanosine exchange complex, the HOPS complex
176 and the WDR81-WDR91 complex, similar to the OC43 and 229E screen results ²². This
177 suggests that endolysosomal host factors can be required for infection under certain
178 conditions but may become largely dispensable for SARS-CoV-2, especially in
179 TMPRSS2-expressing cell types. As nasal and lung epithelial cells can express high
180 levels of TMPRSS2 ⁴¹, we speculate that the genes identified in the SARS-CoV-2
181 CRISPR screen using Huh7.5.1-ACE2-IRES-TMPRSS2 cells may represent rate-limiting

182 factors that are more physiologically relevant to SARS-CoV-2 infection *in vivo* than the
183 endolysosomal components found in our other two screens and in other studies.

184

185 The OC43 and 229E screens also uncovered KEAP1, the principal negative regulator of
186 NRF2, whose activation restores cellular redox and protein homeostasis (Fig. 1c,d) ⁴².

187 Activation of the NRF2 transcriptional program may induce a cellular state that is
188 protective against coronavirus infection. Indeed, NRF2 agonists seem to elicit an antiviral
189 response as demonstrated in cell culture and were proposed for SARS-CoV-2 treatment
190 ^{43,44}.

191

192 In addition to genes that scored in multiple CRISPR screens, we also found genes that
193 were only enriched in one screen. Several genes related to the Golgi apparatus were
194 uncovered only in the 229E screen and may possibly have 229E-specific roles. Among
195 them were GPR89A and GPR89B, which encode two highly homologous G protein
196 coupled receptors important for Golgi acidification ⁴⁵, and NBAS and USE1, which play a
197 role in Golgi-to-ER retrograde transport ⁴⁶. The exact role of these factors in coronavirus
198 infection – and their specificity to 229E – remain to be determined.

199

200 The SARS-CoV-2 screen identified multiple subunits of the exocyst (EXOC1-8) (Fig. 1b,
201 Extended Data Fig. 2a), an octameric protein complex that facilitates the tethering of
202 secretory vesicles to the plasma membrane prior to SNARE-mediated fusion ⁴⁷. This
203 complex could therefore facilitate trafficking of virus particles during entry or egress. The
204 top hit of the SARS-CoV-2 screen was TMEM106B, a poorly characterized lysosomal

205 transmembrane protein linked to frontotemporal dementia (Fig. 1b) ⁴⁸. Deletions in
206 TMEM106B caused defects in lysosome trafficking, impaired acidification and reduced
207 levels of lysosomal enzymes but its precise molecular function remains enigmatic ^{48,49}.
208 TMEM106B KO could thus indirectly affect SARS-CoV-2 entry, although it is also possible
209 that SARS-CoV-2 physically interacts with TMEM106B, for example as lysosomal
210 receptor, similar to NPC1 and LAMP1 for Ebola and Lassa virus, respectively ^{40,50}.

211

212 Overall, the comparative CRISPR screen strategy provides a rich list of shared and
213 distinct candidate host factors for subsequent validation and host-directed inhibition of
214 coronavirus infection.

215

216 Network propagation across multiple CRISPR screens highlights functional biological
217 clusters important for coronavirus infection

218 To better understand the functional connections between the genes identified in our
219 screens, we performed network propagation (Fig. 2b) ⁵¹. This approach integrates large
220 datasets using networks, thereby identifying subnetworks and pathways that are common
221 across datasets. Propagations from the three CRISPR screens identified subnetworks
222 most common to all three viruses and independently confirmed the biological processes
223 highlighted as important for coronavirus infection in our previous analysis (Fig. 2c,
224 Extended Data Fig. 3, Supplementary Table 2 and 3). For instance, we found clusters
225 linked to cholesterol metabolism (containing SCAP, MBTPS1, SREBF2, LDLR and
226 NPC1), endosome to lysosome transport (including the HOPS complex components
227 VPS11, VPS16, VPS18, VPS33A and VPS39) and glycoprotein biosynthetic processes

228 (containing heparan sulfate biosynthesis genes). Another cluster reflected the critical role
229 of autophagy/ phospholipid metabolism and indicated a functional link between VAC14
230 and subunits of the PI3K complex as described above .

231 Moreover, network propagation also identified previously unappreciated biological
232 functions, such as steroid hormone signaling, cell-cell adhesion, metal ion transport, intra-
233 Golgi vesicle transport, snare complex assembly, Rab protein signal transduction,
234 peroxisomal transport and mRNA splicing (Fig. 2c, Extended Data Fig. 3, Supplementary
235 Table 2 and 3). Altogether, network propagation revealed numerous distinct cellular
236 processes that may have critical roles during coronavirus infection.

237

238 Knockout of candidate host factor genes reduces coronavirus replication

239 To validate the candidate genes from the SARS-CoV-2 screen, we generated individual
240 KO cells in two cell types. We first introduced gene deletions for several top hits in A549
241 lung epithelial cells transduced with ACE2 (A549-ACE2) using Cas9 ribonucleoproteins
242 (RNPs) (Extended Data Fig. 4a). SARS-CoV-2 RNA levels were markedly reduced in
243 cells that contained indel mutations in ACE2, the ADP Ribosylation Factor 5 (ARF5),
244 multiple subunits of the exocyst (EXOC2/6/8), the cholesterol homeostasis genes SCAP,
245 MBTPS1 and MBTPS2, the phosphatidylinositol kinase complex components PIKFYVE
246 and VAC14, as well as TMEM106B (Fig. 3a). Additionally, we generated clonal Huh7.5.1
247 cells (without the ACE2-IRES-TMPRSS2 construct) harboring frameshift mutations in a
248 subset of the same genes (Extended Data Fig. 4b). Deletion of TMEM106B and VAC14
249 decreased SARS-CoV-2 replication, and this effect was reversed by cDNA
250 complementation (Fig. 3b,c), thus confirming the role of these two factors in the SARS-

251 CoV-2 life cycle. Similarly, knocking out SCAP, MBTPS2 or EXOC2 led to a decrease of
252 SARS-CoV-2 RNA levels (Fig. 3d). When we infected the same Huh7.5.1 KO cells with
253 HCoV-OC43 and HCoV-229E, we observed reduced viral replication in SCAP and
254 MBTPS2 KO cells, but not in TMEM106B KO and only moderately in VAC14 KO cells
255 (Fig. 3e). This suggests that the latter genes are more rate-limiting in SARS-CoV-2
256 infection.

257

258 Finally, we probed cells lacking several genes involved in endosome maturation or the
259 PI3K complex, which were initially found in the common cold coronavirus screens. We
260 saw reduced viral replication for OC43 and 229E (Fig. 3f,g). Additionally, we observed
261 increased cell viability in all KO cells relative to WT Huh7.5.1 cells 8 dpi, indicating that
262 endosome maturation is important for infection by the common cold viruses and for virus-
263 induced cell death (Extended Data Fig. 4c). Next, we tested whether the hits shared
264 between OC43 and 229E might also affect SARS-CoV-2. Indeed, SARS-CoV-2 infection
265 also depended on endosomal factors in the context of Huh7.5.1 without ACE2-IRES-
266 TMPRSS2, similar to the common cold coronaviruses (Fig. 3h). Additionally, deletions of
267 the PI3K subunits, in particular PIK3R4 KO, led to a strong decrease in replication of all
268 three coronaviruses (Fig. 3h). Together, these experiments confirm that the host factors
269 identified in our screens have functional roles for *Coronaviridae* and demonstrate that
270 important aspects of SARS-CoV-2 biology can be revealed by studying the common cold
271 coronaviruses.

272

273

274 Compounds directed at host factors inhibit coronavirus replication

275 Host factors important for virus infection are potential targets for antiviral therapy. Host-
276 directed therapy is advantageous as it allows pre-existing drugs to be repurposed, it may
277 provide broad-spectrum inhibition against multiple viruses, and it is generally thought to
278 be more refractory to viral escape mutations than drugs targeting viral factors ⁵². We
279 therefore explored whether the cellular pathways identified in our screens could serve as
280 targets for therapy against coronavirus infection.

281

282 Given the strong dependence of all three coronaviruses on PIK3R4, we tested SAR405,
283 a selective and ATP-competitive inhibitor of class III PI3K (PIK3C3) ⁵³. The drug exhibited
284 a dose-dependent effect against all three coronaviruses with low cytotoxicity, consistent
285 with the reduced virus replication in PIK3R4 KO cells, and suggesting that it could serve
286 as a pan-coronavirus inhibitor (Fig. 4a). As VAC14, a PIKfyve complex component, was
287 a strong hit in the SARS-CoV-2 screen, we also tested the PIKfyve inhibitor YM201636
288 and observed inhibition of SARS-CoV-2 replication (Fig. 4b) ⁵⁴. Similar antiviral activity
289 was previously demonstrated with apilimod, another PIKfyve inhibitor ⁵⁵⁻⁵⁷.

290

291 Furthermore, we tested compounds modulating cholesterol homeostasis as this pathway
292 appeared important for all three coronaviruses as well. PF-429242, a reversible,
293 competitive aminopyrrolidineamide inhibitor of MBTPS1 showed dose-dependent
294 reduction of SARS-CoV-2 replication with cytotoxicity only at high concentration (Fig. 4c)
295 ⁵⁸. Fatostatin, which binds to SCAP and inhibits ER-to-Golgi translocation of SREBPs,
296 also moderately reduced SARS-CoV-2 infection levels at higher doses (Fig. 4d) ⁵⁹. The

297 two cholesterol modulating compounds also led to a decrease in OC43 and 229E levels,
298 suggesting that modulation of intracellular cholesterol levels could be used as pan-
299 coronavirus treatment (Fig. 4e). Therefore, our genetic and pharmacological data suggest
300 that both phosphatidylinositol kinase complexes and cholesterol homeostasis are
301 potential targets for pan-coronavirus host-directed therapy in vitro and may be explored
302 further in vivo.

303

304 **Discussion**

305 In this study, we performed genome-scale CRISPR KO screens to identify host factors
306 important for SARS-CoV-2, HCoV-229E and HCoV-OC43. Our data highlight that while
307 the three coronaviruses exploit distinct entry factors, they also depend on a convergent
308 set of host pathways, with potential roles for the entire *Coronaviridae* family. In particular,
309 genes involved in cholesterol homeostasis were enriched in all screens and in the network
310 propagation. Consistent with our data, two SARS-CoV-2 interactomes revealed binding
311 of viral proteins to SCAP, and a recent CRISPR screen focused on the interactome
312 components also identified SCAP as a host factor critical for SARS-CoV-2 replication
313 ^{16,17,21}; given the essentiality of SCAP for replication, viral proteins are likely to positively
314 regulate SCAP activity and cholesterol levels. Cellular cholesterol homeostasis has
315 previously been linked to viral entry and membrane fusion in the context of bunya- and
316 hantavirus infections, suggesting a pro-viral function across different viral families ^{60–62}.
317 Consistent with this hypothesis, treatment with 25-hydroxycholesterol, which blocks
318 SREBP processing and stops cholesterol synthesis, reduced infection with SARS-CoV-1
319 and CoV-2 spike-pseudotyped viruses ^{29,63}.

320 Additionally, phosphatidylinositol biosynthesis was uncovered as an important pathway
321 for coronavirus infection. While PIKfyve has previously been implicated through chemical
322 inhibition ^{55–57}, we identified the upstream PI3K complex as a new critical host factor,
323 potentially exhibiting pan-coronavirus function. Due to its involvement in multiple cellular
324 processes including vesicular trafficking and autophagy ²⁸, it remains to be determined
325 whether coronaviruses hijack this pathway during entry or for the generation of double-
326 membrane vesicles required for the viral replication/transcription complexes.

327

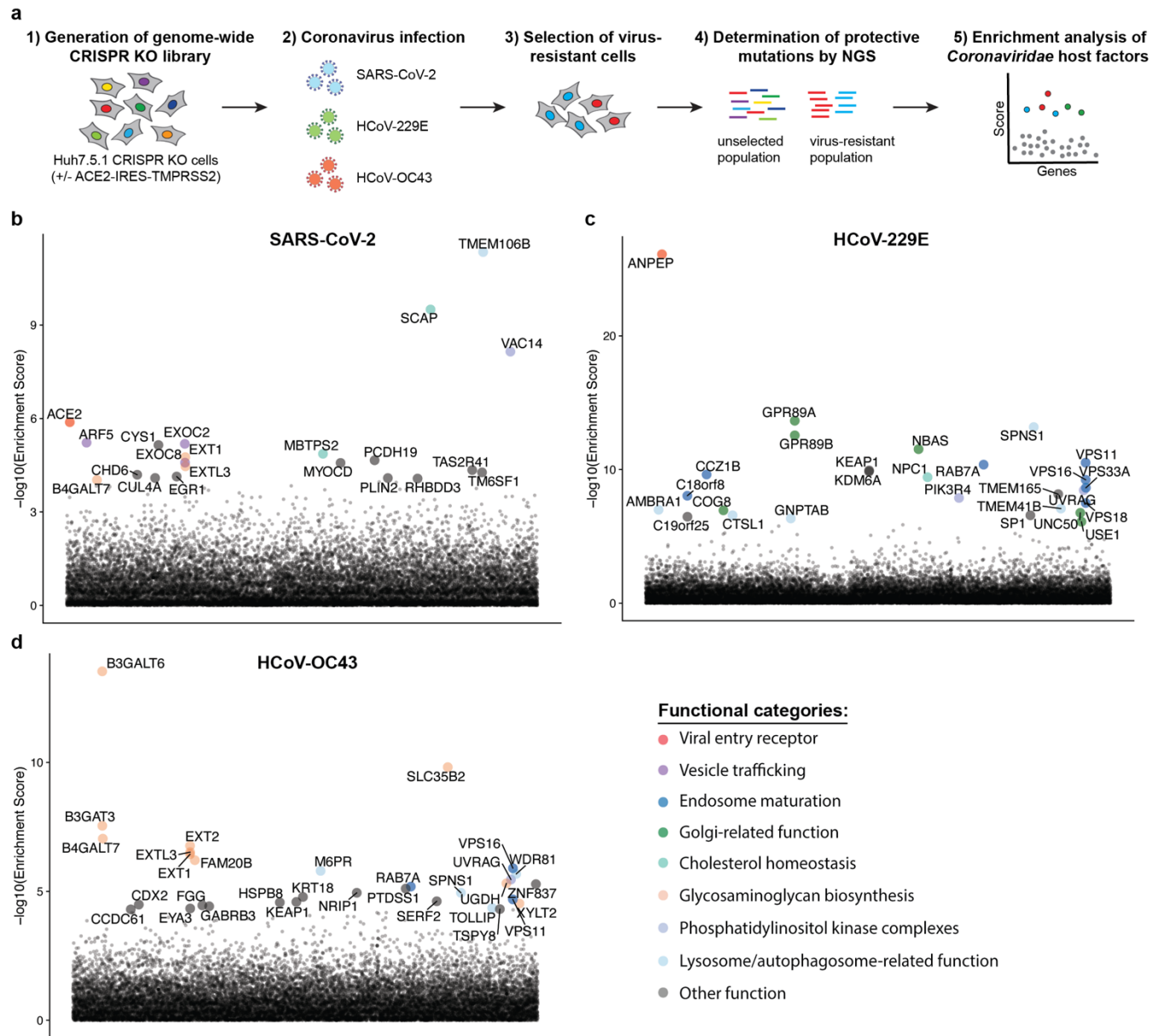
328 Our results also inform those of a recent drug repurposing screen, which identified ~100
329 compounds that inhibited SARS-CoV-2 replication ⁶⁴; notably, among those were PIKfyve
330 inhibitors, protease inhibitors and modulators of cholesterol homeostasis. Our functional
331 genomics data therefore suggest that the observed effects of several compounds were
332 possibly due to inhibition of critical host factors.

333

334 In conclusion, our study offers important insight into host pathways commonly hijacked
335 by coronaviruses. Importantly, the identification of the phosphatidylinositol PIK3C3 kinase
336 complex as a potent therapeutic target for SARS-CoV-2 based on the 229E and OC43
337 screens underscores the value of the parallel CRISPR screening approach for finding
338 novel therapies against SARS-CoV-2 and other *Coronaviridae*.

339

Figure 1



340

341 **Figure 1: Genome-wide CRISPR KO screens in human cells identify host factors**

342 **important for infection by for SARS-CoV-2, HCoV-229E and HCoV-OC43. (a)**

343 Schematic of CRISPR KO screens for the identification of coronavirus host factors.

344 Huh7.5.1-Cas9 (with bicistronic ACE2-IRES-TMPRSS2 construct for SARS-CoV-2 and

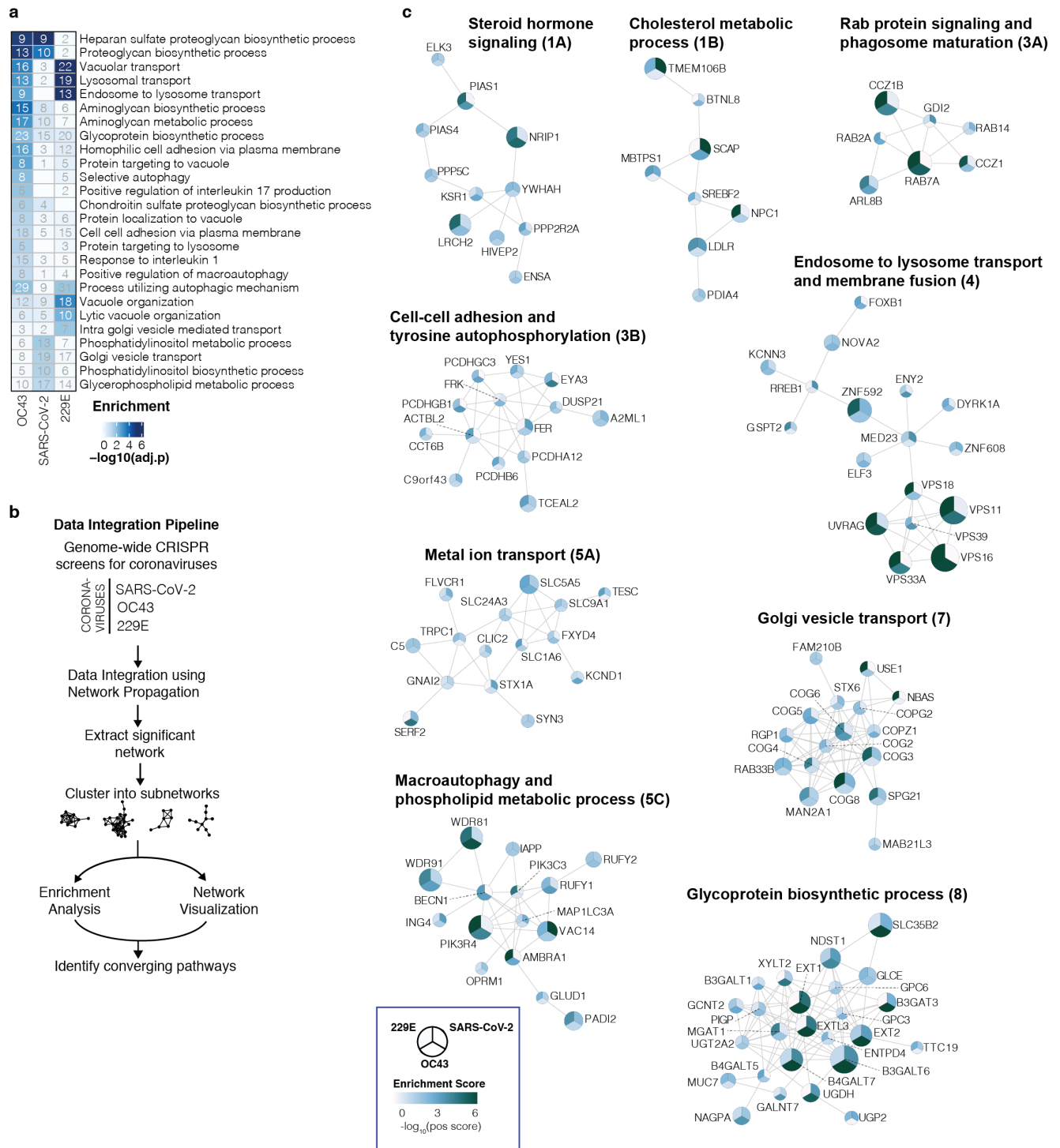
345 without for 229E and OC43 screen) were mutagenized using a genome-wide sgRNA

346 library. Mutant cells were infected with each coronavirus separately and virus-resistant

347 cells were harvested 10-14 days post infection (dpi). The abundance of each sgRNA in
348 the starting and selected population was determined by high-throughput sequencing and
349 a gene enrichment analysis was performed. **(b-d)** Gene enrichment of CRISPR screens
350 for **(b)** SARS-CoV-2, **(c)** 229E and **(d)** OC43 infection. Enrichment scores were
351 determined by MaGECK analysis and genes were colored by biological function. The
352 SARS-CoV-2 was performed once. The 229E and OC43 screens were performed twice
353 and combined MaGECK scores are displayed.

354

Figure 2



355

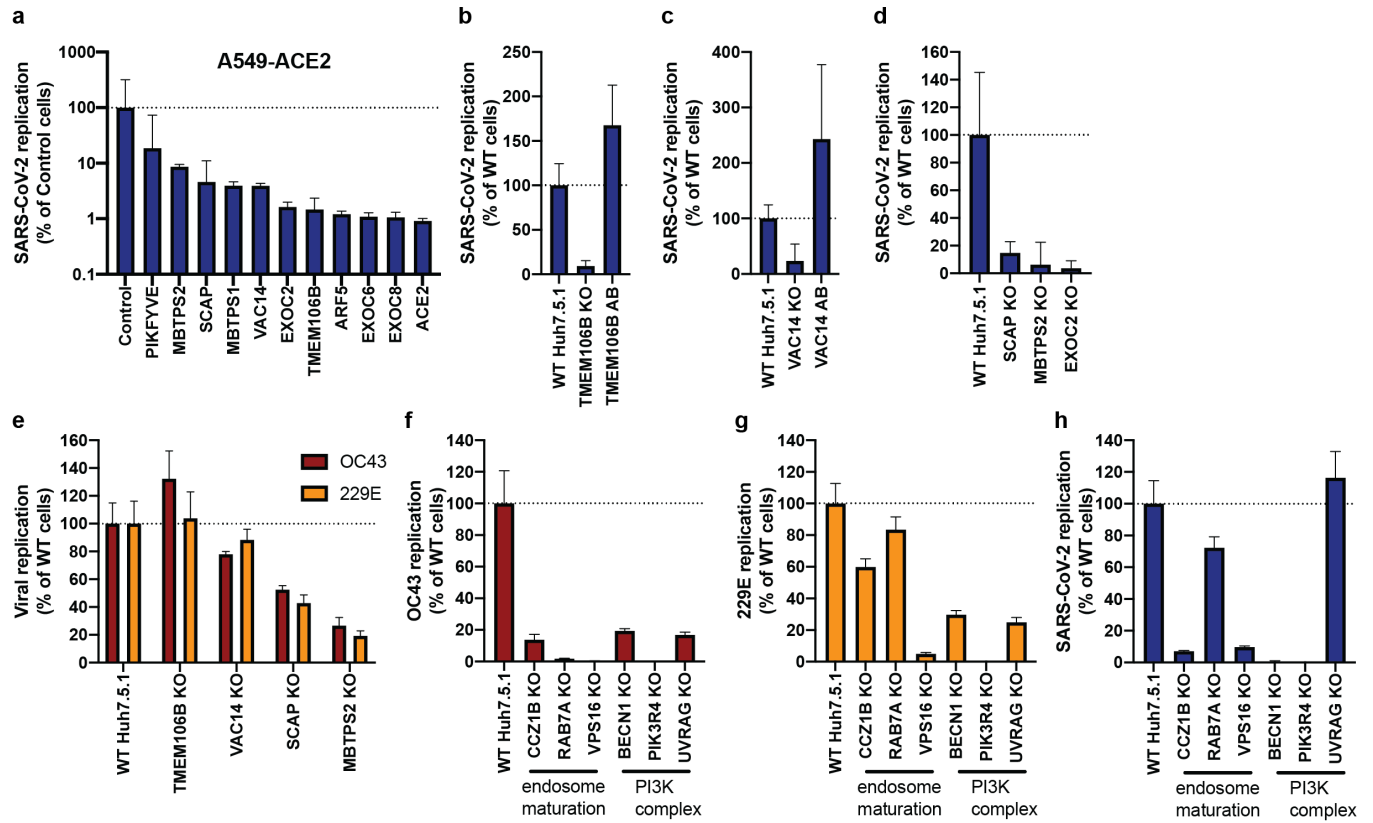
356 **Figure 2: Gene ontology analysis and network propagation highlight pathways and**

357 **biological signaling networks important for coronavirus infection. (a) Gene ontology**

358 (GO) enrichment analysis was performed on significant hits from the individual CRISPR
359 screens (MaGECK enrichment score ≤ 0.005). P values were calculated by
360 hypergeometric test and a false-discovery rate was used to account for multiple
361 hypothesis testing. The top GO terms of each screen were selected for visualization. **(b)**
362 Data integration pipeline for network propagation of identified host factor genes.
363 Unthresholded positive enrichment scores served as initial gene labels for network
364 propagation using Pathway Commons. Separately propagated networks were integrated
365 gene-wise (via multiplication) to identify biological networks that are shared between all
366 three datasets. Genes found to be significant in the propagation (see Methods) were
367 extracted, clustered into smaller subnetworks, and annotated using GO enrichment
368 analysis. **(c)** Selected biological subnetwork clusters from network propagation. Cluster
369 title indicates the most significant biological function(s) for each cluster. Circle size
370 represents p-value from network propagation permutation test (see Methods). The
371 original positive enrichment score of a gene in each CRISPR screen is indicated by color
372 scale within the circle. The entire set of identified clusters is displayed in Extended Data
373 Fig. 3a. (#) is the cluster number, which refers to the enrichment analysis of biological
374 processes in Extended Data Fig. 3b and Supplementary Table 2.

375

Figure 3



376

377 **Figure 3: Knockout of candidate host factor genes reduces coronavirus infection.**

378 **(a)** RT-qPCR quantification of intracellular SARS-CoV-2 levels in RNP edited A549-ACE2

379 cells. Cells were infected using moi=0.01 and harvested at 72 hours post infection (hpi).

380 **(b-d)** RT-qPCR quantification of intracellular SARS-CoV-2 levels in WT Huh7.5.1 cells or

381 cells harboring frameshift mutations or frameshift mutant cells complemented with

382 respective cDNAs. Cells were infected using moi=0.01 and harvested at 24 hpi. **(e-g)** RT-

383 qPCR quantification of intracellular OC43 and 229E RNA levels in WT and KO Huh7.5.1

384 cells. Cells were infected using moi=0.05 (229E) and moi=3 (OC43) and harvested at 48

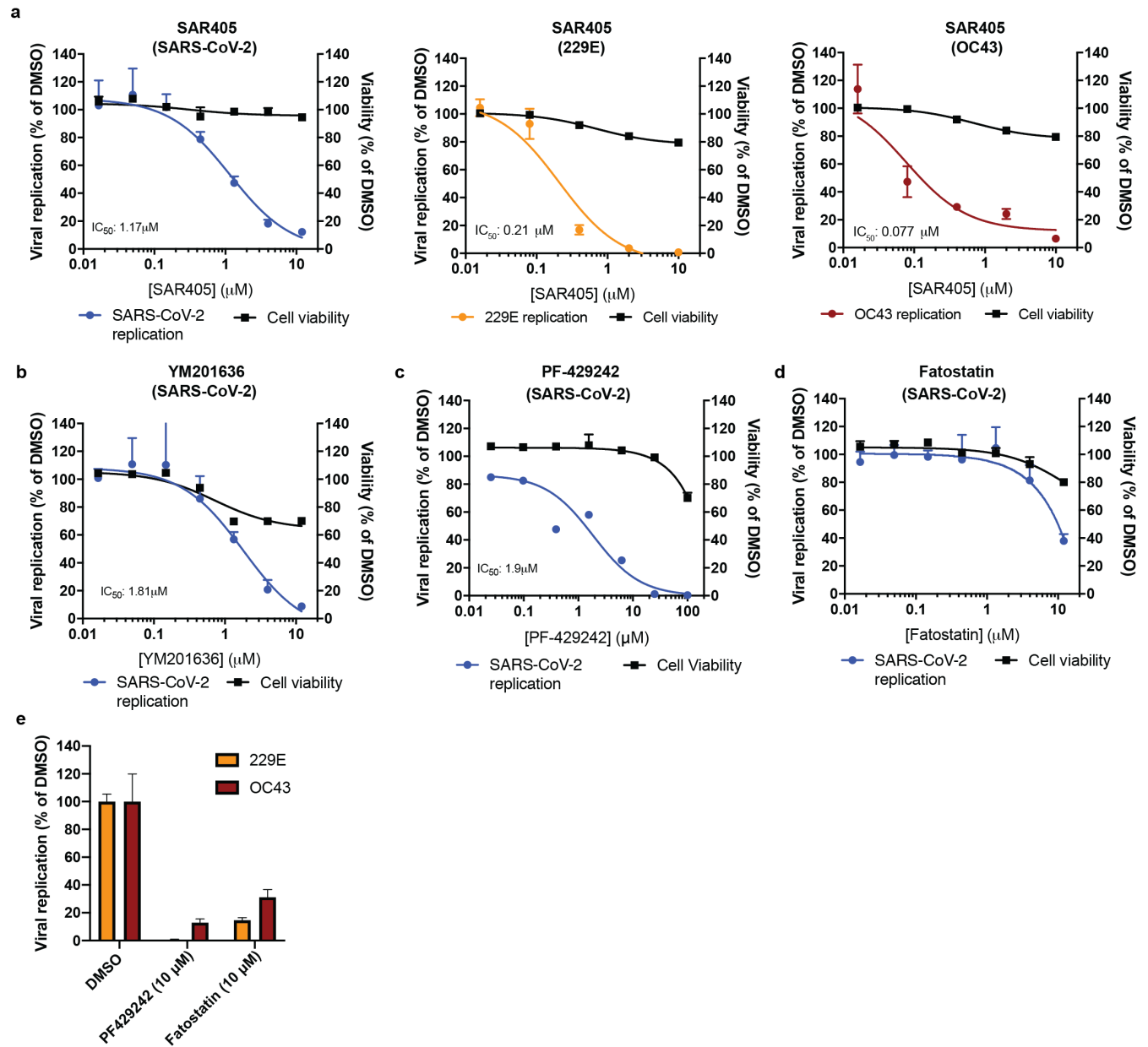
385 hpi. **(h)** RT-qPCR quantification of intracellular SARS-CoV-2 levels in Huh7.5.1 WT or KO

386 cells by RT-qPCR. Cells were infected using moi=0.01 and harvested at 24 hpi.

387 For SARS-CoV-2 infection, viral transcripts were normalized to cellular RNaseP. For
388 OC43 and 229E experiments, viral RNA was normalized to 18S RNA. For all RT-qPCR
389 experiments, results are displayed relative to infection in WT cells and data represent
390 means \pm s.e.m. from 3 biological samples.

391

Figure 4



392

393 **Figure 4: Pharmacological inhibition of phosphatidylinositol kinase complexes and**

394 **cellular cholesterol homeostasis decreases infection with SARS-CoV-2 and**

395 **common cold coronaviruses. (a) SAR405 dose-response curves for SARS-CoV-2,**

396 **HCoV-229E and HCoV-OC43 replication in Huh7.5.1 cells and for cell viability of drug**

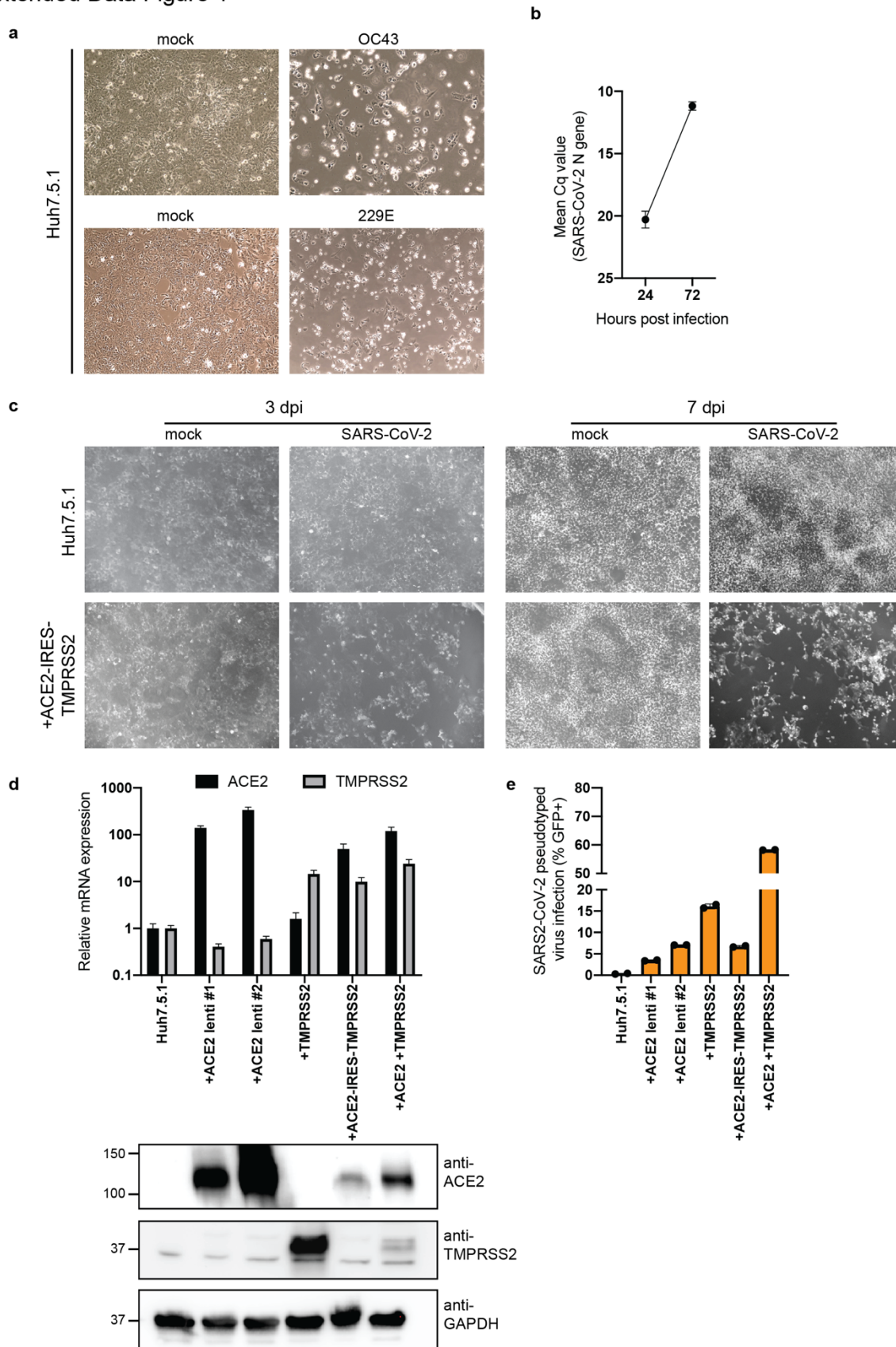
397 **treated cells. (b-d) Dose-response curves of the effect of (b) YM201636, (c) PF-429242,**

398 and **(d)** fatostatin to on SARS-CoV-2 replication in Huh7.5.1 cells and on cell viability of
399 drug treated cells. **(e)** Quantification of 229E and OC43 replication in the presence of PF-
400 429242 or fatostatin.

401 For all experiments, compounds were added simultaneously with virus. Viral RNA was
402 quantified after 24 hpi (SARS-CoV-2) or 48hpi (229E and OC43) using RT-qPCR and
403 normalized to RnaseP (SARS-CoV-2) or 18S RNA (229E and OC43). Values represent
404 means \pm s.e.m. relative to DMSO treated cells. For cell viability, datasets represent means
405 \pm s.d. and values are relative to DMSO treated uninfected controls. Non-linear curves
406 were fitted with least squares regression using GraphPad Prism 8 and IC₅₀ was
407 determined for (a-c). All experiments were performed in 3 biological replicates.

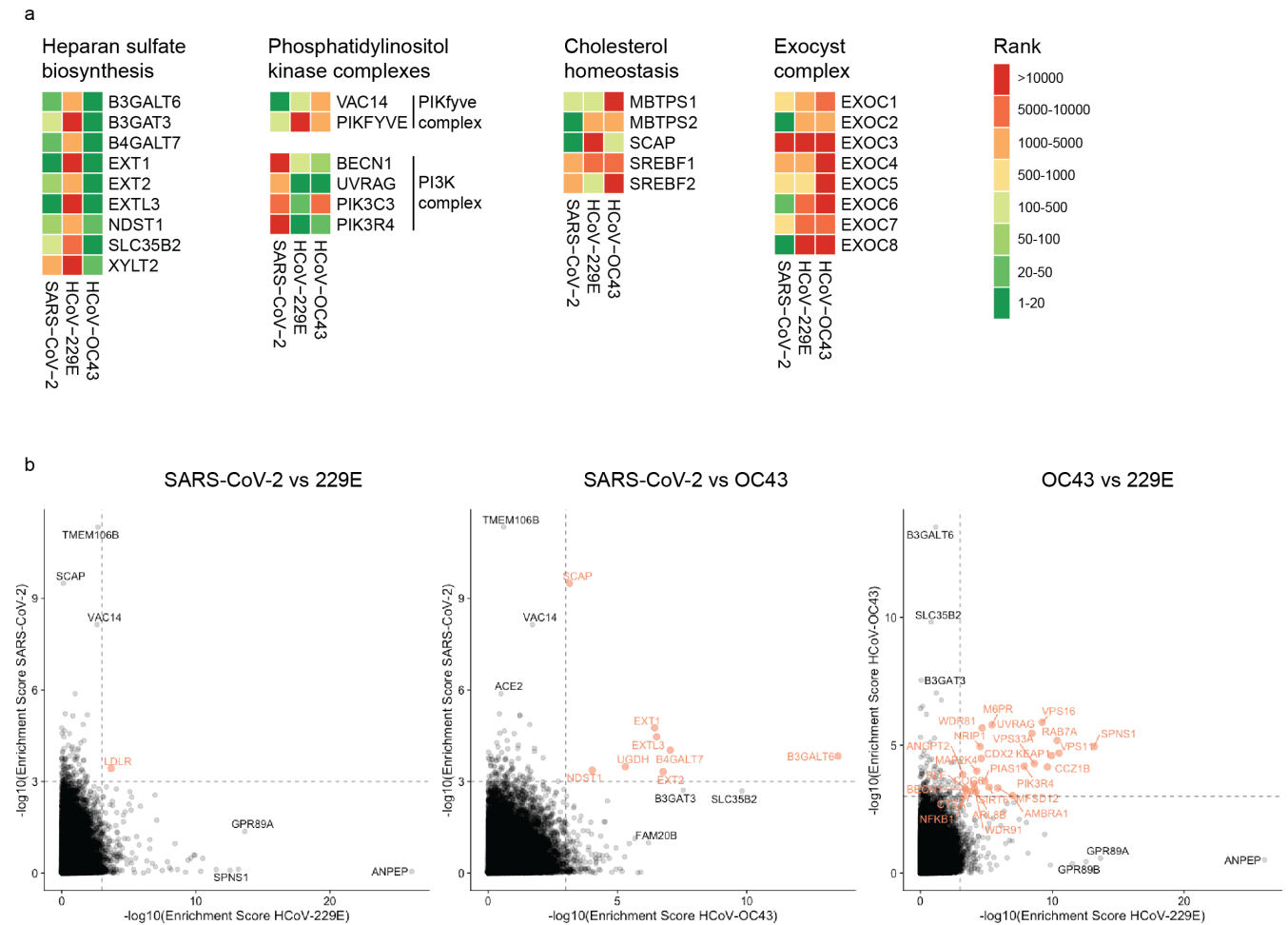
408

Extended Data Figure 1



410 **Extended Data Figure 1: Huh7.5.1 cells are susceptible to SARS-CoV-2, HCoV-OC43**
411 **and HCoV-229E. (a)** Light microscopy images of WT Huh7.5.1 infected with OC43 (7 dpi)
412 and 229E (4 dpi). **(b)** Quantification of SARS-CoV-2 RNA in WT Huh7.5.1 cells at 24 and
413 72 hpi by RT-qPCR. Cq values represent mean \pm s.e.m. from 3 biological replicates. **(c)**
414 Light microscopy images of SARS-CoV-2 infected WT Huh7.5.1 cells or Huh7.5.1 cells
415 expressing ACE2-IRES-TMPRSS2 at 3 and 7 dpi. **(d)** Quantification of ACE2 and
416 TMPRSS2 expression in WT and lentivirally transduced Huh7.5.1 cells by RT-qPCR and
417 Western blot. mRNA levels are displayed as mean \pm s.e.m. from two independent
418 harvests and are relative to expression in WT cells. Anti-ACE2 and anti-TMPRSS2
419 antibodies were used to detect protein levels in WT and overexpression cells. GAPDH
420 was used as loading control. Molecular weight markers are indicated on the left. **(e)**
421 Quantification of infection with pseudotyped lentivirus bearing SARS-CoV-2 spike and
422 expressing a GFP by flow cytometry. Values are from two biological samples and are
423 displayed as means \pm s.d.

Extended Data Figure 2



424

425 **Extended Data Figure 2: Comparison of CRISPR screens reveals common and**

426 **distinct host factors across SARS-CoV-2, 229E and OC43. (a) CRISPR screen**

427 **ranking of genes, which are part of specific cellular pathway or complexes, across the**

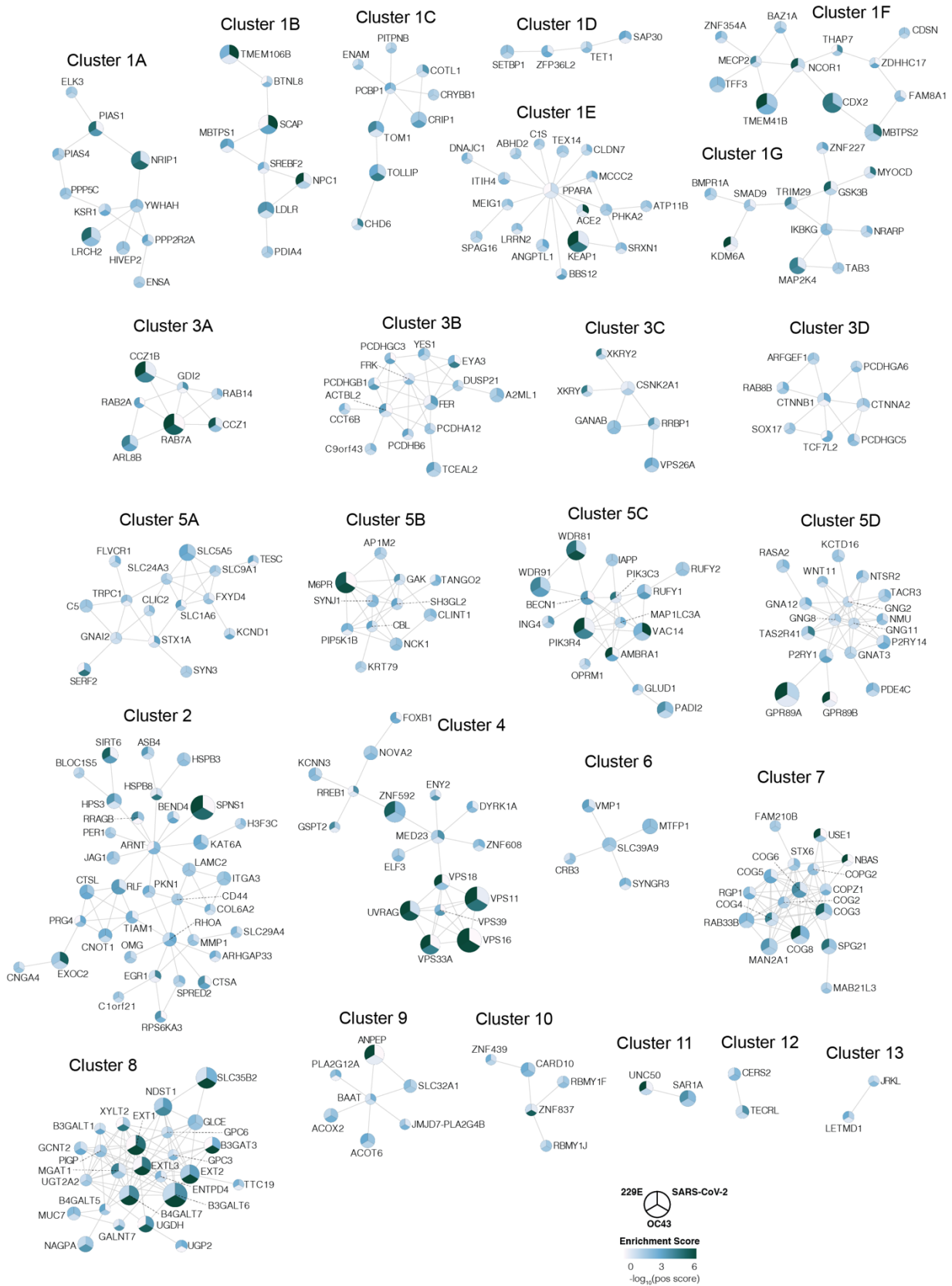
428 **three CRISPR screens. (b) Pairwise comparisons of gene enrichments between two**

429 **CRISPR screens. Dotted lines indicate $-\log_{10}(\text{Enrichment score}) > 3$. Genes that scored**

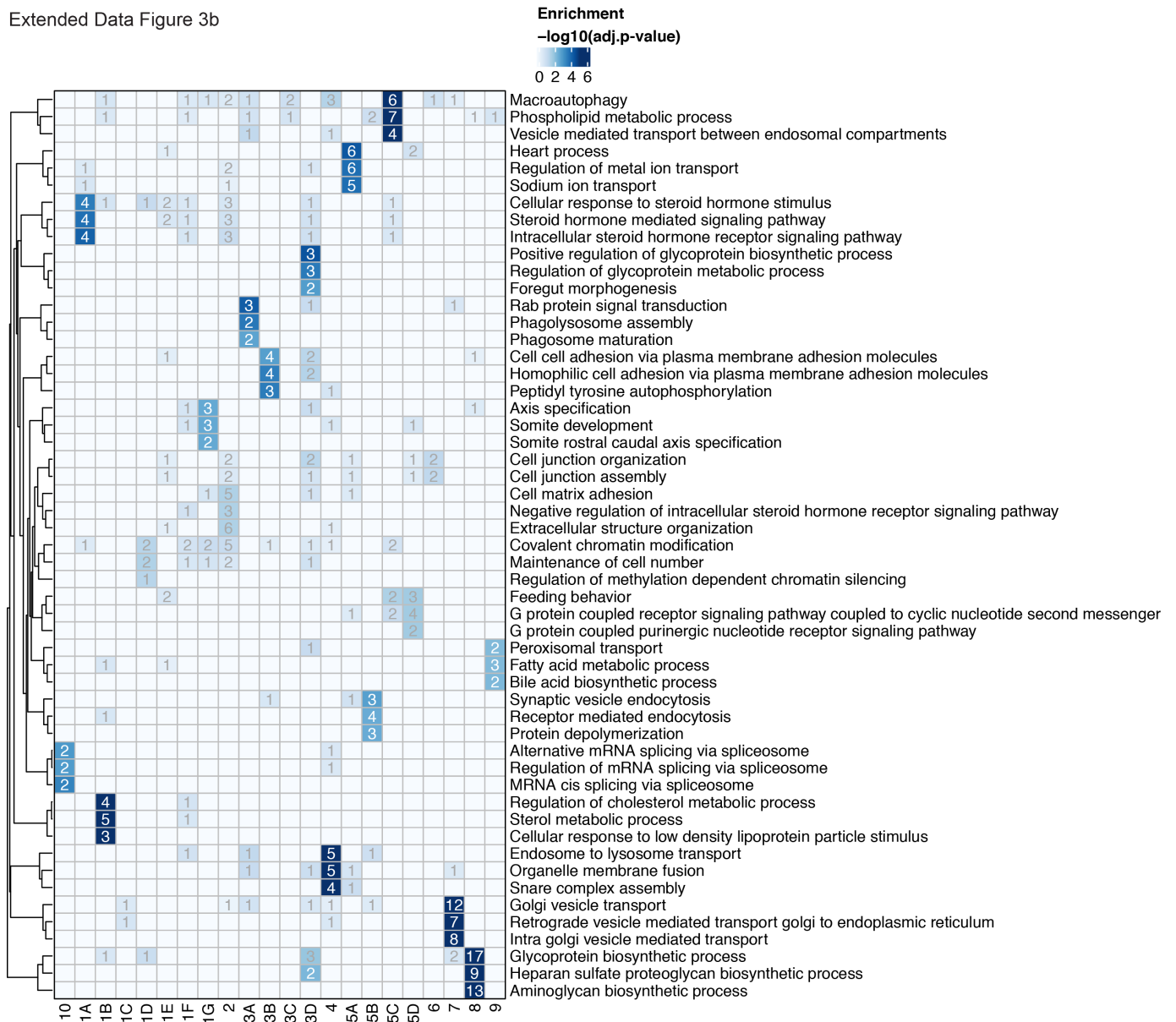
430 **above the threshold in both screens, are highlighted in red.**

431

Extended Data Figure 3a



Extended Data Figure 3b



433

434 **Extended Data Figure 3: Network propagation of CRISPR screen hits reveals**

435 **functional clusters with distinct biological functions. (a) Biological subclusters from**

436 network propagation. Cluster number refers to the enrichment analysis of biological

437 processes for each cluster, displayed in Extended Data Fig. 3b. Circle size represents p-

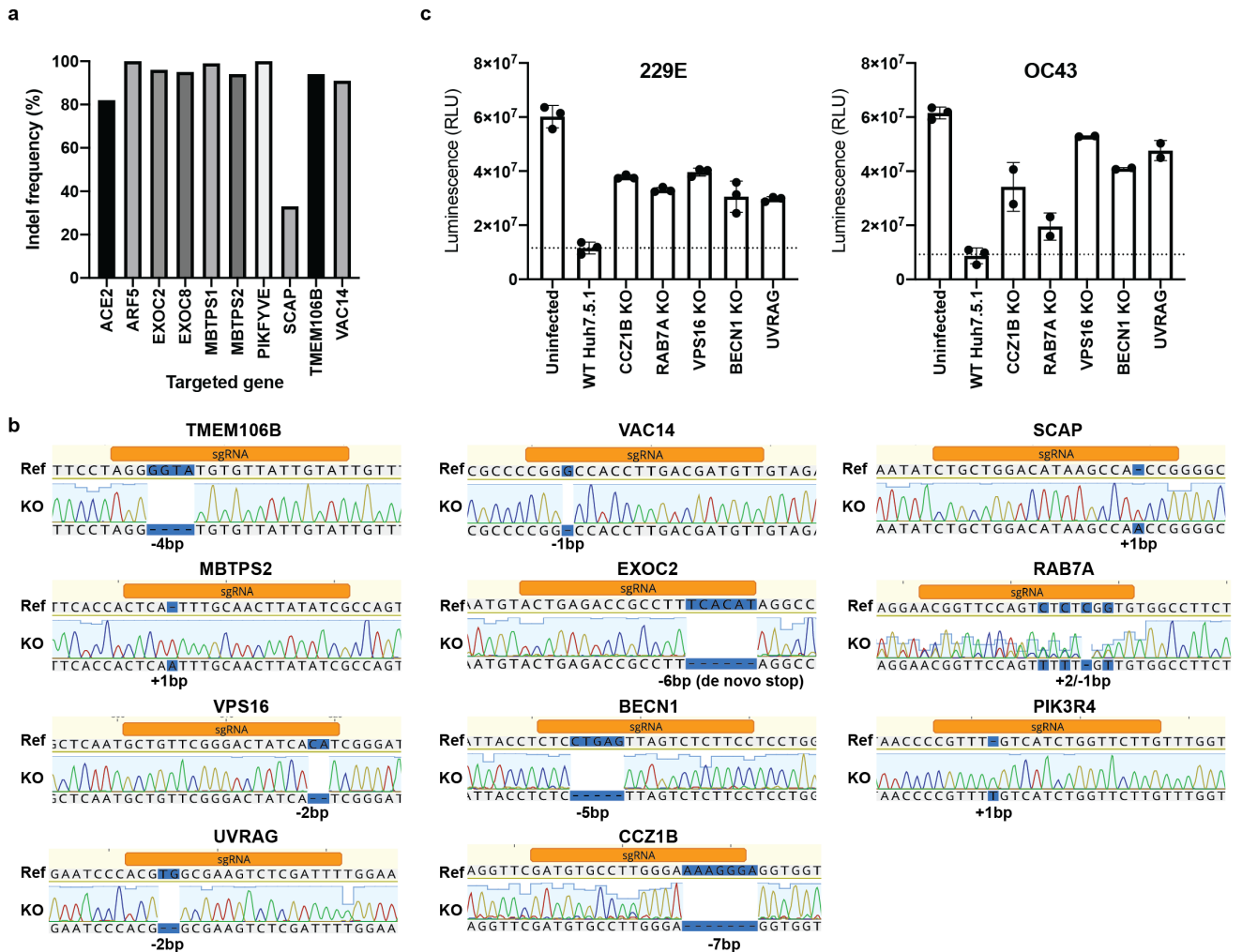
438 value from integrative network propagation permutation test (gene-wise multiplication

439 across datasets, see Methods). The original positive enrichment score of a gene in each

440 CRISPR screen is indicated by color scale within the circle. (b) Gene ontology (GO)

441 enrichment analysis was performed on each subcluster from the network propagation. P
442 values were calculated by hypergeometric test and a false-discovery rate was used to
443 account for multiple hypothesis testing. The entire set of enriched biological processes
444 for each subcluster is listed in Supplementary Table 2.
445

Extended Data Figure 4



446

447 **Extended Data Figure 4: Knockout of host factor genes reduces coronavirus**

448 **infection and virus-induced cell death. (a)** Indel frequency of RNP-edited polyclonal

449 A549-ACE2 KO cells. Targeted loci were PCR-amplified, Sanger-sequenced and

450 analyzed using Inference of CRISPR Edits (ICE) analysis⁶⁵. **(b)** Genotyping of clonal

451 Huh7.5.1. Targeted loci were PCR-amplified, Sanger-sequenced and aligned to WT

452 reference sequence. Frameshifts are highlighted in blue. **(c)** Cell viability measurement

453 of 229E or OC43 infected WT and KO Huh7.5.1 cells. Cells were infected with 229E

454 (moi=0.05) or OC43 (moi=3) and viability was determined 8 dpi using Cell Titer Glo.

455 Values are displayed as means \pm s.d. from three (229E) or two (OC43) biological
456 samples.

457

458 **Material and Methods:**

459 Cell culture

460 Huh7.5.1 (gift from Frank Chisari), HEK293FT (Thermo Scientific), Vero cells (ATCC) and
461 A549-ACE2 cells (gift from Olivier Schwartz) were cultured in DMEM (Gibco)
462 supplemented with 10% fetal bovine serum (FBS, Omega Scientific),
463 penicillin/streptomycin (Gibco), non-essential amino acids (Gibco) and L-glutamine
464 (Gibco) at 37C and 5% CO₂. Cell lines were tested negative for mycoplasma
465 contamination.

466

467 Plasmids, cloning and lentivirus production

468 The following cDNA sequence containing plasmids were obtained: hACE2 (Addgene,
469 #1786, gift from Hyeryun Choe), TMPRSS2 (Addgene, #53887, gift from Roger Reeves),
470 TMEM106B (Genscript, OHu17671) and VAC14 (Addgene, #47418, gift from Peter
471 McPherson).

472 Individual cDNAs were cloned into EcoRV-cut plenti-CMV-Puro-DEST Addgene, #17452,
473 gift from Eric Campeau & Paul Kaufman) or plenti-CMV-Hygro-DEST (Addgene, #17454,
474 gift from Eric Campeau & Paul Kaufman) using NEBuilder HiFi DNA Assembly Master
475 Mix (NEB). To generate the plenti-CMV-ACE2-IRES-TMPRSS2 construct, ACE2, EMCV
476 IRES (derived from pLenti-DsRed_IRES_EGFP (Addgene, #92194, gift from Huda
477 Zoghbi)), and TMPRSS2 were individually amplified with addition of overlapping
478 sequences and the three fragments were assembled using NEBuilder HiFi DNA
479 Assembly Master Mix.

480 Lentivirus was produced in HEK293FT by co-transfection of cDNA containing lentiviral
481 plasmid together with pCMV-dR8.2 dvpr (Addgene, #8455, gift from Bob Weinberg),
482 pCMV-VSV-G (Addgene, #8454, gift from Bob Weinberg) and pAdVantage (Promega)
483 using FugeneHD (Promega). Supernatants were collected 48h post-transfection, filtered
484 and added to recipient cells in presence of Polybrene (SCBT). Transduced cells were
485 subsequently selected using Puromycin or Hygromycin for 5-7 days.

486

487 Virus propagation and titration

488 HCoV-OC43 was obtained from ATCC (VR-1558) and propagated in Huh7.5.1 cells at
489 33C. HCoV-229E was obtained from ATCC (VR-740) and propagated in Huh7.5.1 cells
490 at 33C. SARS-CoV-2 (USA/WA-1/2020 strain) was obtained through BEI Resources (NR-
491 52281) and propagated in Vero cells. Supernatants were collected when cytopathic effect
492 was apparent, filtered and stored at -80C. Viral titers were determined by standard plaque
493 assay using either Huh7.5.1 cells (OC43 and 229E) or Vero cells (SARS-CoV-2). Briefly,
494 serial 10-fold dilutions of virus stocks were used to infect cells in 6-well plates for 1h and
495 an overlay of DMEM media containing 1.2% Avicel RC-591 was added. Cells were
496 incubated for 3-4 days, followed by fixation with 10% formaldehyde, staining with crystal
497 violet and plaque counting. Additionally, SARS-CoV-2 stock was sequence-verified by
498 next-generation sequencing. All experiments with OC43 and 229E were performed in a
499 biosafety level 2 laboratory and all experiments involving SARS-CoV-2 were performed
500 in a biosafety level 3 laboratory.

501

502

503 Genome-wide CRISPR screens

504 Huh7.5.1-Cas9 cells were generated by lentiviral transduction with lentiCas9-blast
505 (Addgene, #52962, gift from Feng Zhang) and subsequently selected with blasticidin for
506 7 days. A portion of Huh7.5.1-Cas9 cells were additionally transduced with lentivirus
507 containing ACE2-IRES-TMPRSS2-hygro. To generate CRISPR KO libraries, a total of
508 240 million Huh7.5.1-Cas9-blast or Huh7.5.1-Cas9-blast+ACE2-IRES-TMPRSS2-hygro
509 cells were transduced with lentivirus of the human GeCKO v2 library (Addgene,
510 #1000000049, gift from Feng Zhang) at a moi of 0.4 and subsequently selected using
511 puromycin and expanded for 7 days. A total of 60 million mutagenized cells for each
512 GeCKO sublibrary (A and B) were collected for genomic DNA extraction to assess the
513 sgRNA representation of the starting population. For the SARS-CoV-2 CRISPR host
514 factor screen, 100 million cells of Huh7.5.1-Cas9-blast+ACE2-IRES-TMPRSS2-hygro
515 GeCKO library cells were infected with SARS-CoV-2 at a multiplicity of infection (moi) of
516 0.01. Virus-induced cell death was apparent after 2-3 days and surviving cells were
517 collected 12 dpi. The screen was performed once.

518 For the 229E and OC43 CRISPR screens, 100 million cells (per screen) of Huh7.5.1-
519 Cas9-blast GeCKO library cells were infected with 229E and OC43 at moi of 0.05 and 3,
520 respectively. Cells were incubated at 33C to increase CPE, which was apparent after 3-
521 4 days. Surviving cells were collected after 10 days for 229E and 14 days for OC43. Each
522 screen was performed in two replicates. For all CRISPR screens, genomic DNA (gDNA)
523 was extracted using either QIAamp DNA Blood Maxi Kit (Qiagen) or Quick-DNA Midiprep
524 Plus (Zymo). The sgRNA expression cassettes were amplified from gDNA in a two-step
525 nested PCR using KAPA HiFi HotStart ReadyMixPCR Kit (Kapa Biosystems). For PCR1,

526 40 reactions (for control samples) and 10-16 reactions (for virus selected samples)
527 containing 4 µg gDNA were set up and amplified for 16 cycles. Reactions were pooled,
528 mixed and 200 µl were cleaned up using QIAquick PCR Purification kit (Qiagen). For
529 PCR2, 3 reactions containing 5 µl PCR1 product were amplified for 12 cycles using
530 indexed primers. PCR products were gel purified using QIAquick Gel Extraction Kit
531 (Qiagen) and sequenced on an Illumina NextSeq 500 using a custom sequencing primer.
532 Primers sequences are listed in Supplementary Table 4.

533 Demultiplexed FASTQ files were aligned to a reference table containing sgRNA
534 sequences and abundance of each sgRNA was determined for each starting and selected
535 cell population. Guide count tables were further processed using MaGECK with default
536 “norm-method” to determine positive enrichment scores for each gene⁶⁶. For 229E and
537 OC43, two biological screen replicates were used as input, and for SARS-CoV-2, one
538 biological screen replicate was used. The gene ontology enrichment of the individual
539 screens was run on genes with MaGECK positive score ≤ 0.005 using the GO Biological
540 Processes of the Molecular Signatures Database (MSigDB).

541

542 Network propagation

543 We performed network propagation analysis for the three virus CRISPR screens using
544 the Pathway Commons network⁶⁷. Specifically, we used a heat-diffusion kernel
545 analogous to random walk with restart (RWR, also known as insulated diffusion and
546 personalized PageRank) which better captures the local topology of the interaction
547 network compared to a general heat diffusion process. The process is captured by the
548 steady-state solution as follows:

549
$$P_{SS} = \alpha(I - (1 - \alpha)W)^{-1}P_0$$

550 where P_{SS} represents the vector of propagated values at steady-state, P_0 is the initial
551 labeling (genes of interest from molecular studies), W is the normalized version of the
552 adjacency matrix of the underlying network (in this implementation $W = AD^{-1}$, where A is
553 the unnormalized adjacency matrix, and D is the diagonal degree matrix of the network),
554 I is the identity matrix, and α denotes the restart probability (here, $\alpha=0.2$), which is the
555 probability of returning to the previously visited node, thus controlling the spread through
556 the network.

557 We performed three independent propagations, one for each CRISPR dataset (i.e. each
558 virus). After propagation, each propagated network was integrated by multiplying gene-
559 wise. Such an operation is used to create a gene list ranked to prioritize genes with high
560 scores from all propagated datasets. To control for nodes with high degree (i.e. many
561 connections), which due to their heightened connectivity are biased to receive higher
562 propagation scores, we conducted a permutation test. Specifically, we simulated random
563 propagations by shuffling the positive scores to random genes, repeating this 20,000
564 times per CRISPR screen. Next, we calculated an empirical p-value by calculating the
565 fraction of random propagation runs greater than or equal to the true propagation run for
566 each gene.

567 The network was created by extracting a subnetwork from the same Pathway Commons
568 network corresponding to genes possessing a significant p-value ($p \leq 0.01$) from the
569 propagation ($n=378$). Of these, interconnected genes were visualized using Cytoscape
570 ($n=284$). The resulting network was clustered into subnetworks using the GLay
571 Cytoscape plugin⁶⁸. Three large clusters (1, 3, and 5) were further clustered using GLay

572 into additional subclusters (denoted with letters), resulting in a total of 25 subnetwork
573 clusters (see Extended Data Fig. 3a and Supplementary Table 3). Lastly, Gene Ontology
574 (GO) enrichment analysis (biological process) was performed for each of the 25 resulting
575 subclusters to identify biological processes and pathways associated with each
576 subcluster.

577

578 Generation of clonal Huh7.5.1 KO cell lines

579 sgRNA sequences against gene targets were designed using the GPP sgRNA Designer
580 (<https://portals.broadinstitute.org/gpp/public/analysis-tools/sgrna-design>). DNA oligos
581 (IDT) containing sgRNA sequences were annealed and ligated into pX458 (Addgene,
582 #48138, gift from Feng Zhang). Cells were transfected with pX458 constructs using Mirus
583 TransIT-X2 (Mirus Bio) and two days later GFP positive cells were single-cell sorted into
584 96-well plates using a Sony SH800 cell sorter. For genotyping, genomic DNA was isolated
585 from obtained clones using DNA QuickExtract (Lucigen), the sgRNA-targeted sites PCR
586 amplified and the products Sanger-sequenced. Obtained sequences were compared to
587 reference sequences and clones containing a frameshift indel or de novo stop codon were
588 selected. A list of all used sgRNA sequences and genotyping primers can be found in
589 Supplementary Table 4.

590

591 Generation of RNP edited A549-ACE2 cells

592 sgRNAs were designed according to Synthego's multi-guide gene knockout. Briefly, two
593 or three sgRNAs are bioinformatically designed to work in a cooperative manner to
594 generate small, knockout-causing, fragment deletions in early exons. These fragment

595 deletions are larger than standard indels generated from single guides. The genomic
596 repair patterns from a multi-guide approach are highly predictable based on the guide-
597 spacing and design constraints to limit off-targets, resulting in a higher probability protein
598 knockout phenotype.

599 RNA oligonucleotides were chemically synthesized on Synthego solid-phase synthesis
600 platform, using CPG solid support containing a universal linker. 5-Benzylthio-1H-tetrazole
601 (BTT, 0.25 M solution in acetonitrile) was used for coupling, (3-((Dimethylamino-
602 methylidene)amino)-3H-1,2,4-dithiazole-3-thione (DDTT, 0.1 M solution in pyridine) was
603 used for thiolation, dichloroacetic acid (DCA, 3% solution in toluene) for used for
604 detritylation. Modified sgRNA were chemically synthesized to contain 2'-O-methyl
605 analogs and 3' phosphorothioate nucleotide interlinkages in the terminal three nucleotides
606 at both 5' and 3' ends of the RNA molecule. After synthesis, oligonucleotides were subject
607 to series of deprotection steps, followed by purification by solid phase extraction (SPE).
608 Purified oligonucleotides were analyzed by ESI-MS.

609 To induce gene knockout, 5 pmol Streptococcus Pyogenes NLS-Sp.Cas9-NLS (SpCas9)
610 nuclease (Aldevron) was combined with 15 pmol total synthetic sgRNA (5 pmol each
611 sgRNA) (Synthego) to form ribonucleoproteins (RNPs) in 20uL total volume with SE
612 Buffer (Lonza). The RNP assembly reaction was mixed by pipetting up and down and
613 incubated at room temperature for 10 minutes.

614 All cells were dissociated into single cells using TrypLE Express (Gibco), as described
615 above, resuspended in culture media and counted. 100,000 cells per nucleofection
616 reaction were pelleted by centrifugation at 200 xg for 5 minutes. Following centrifugation,
617 cells were resuspended in transfection buffer according to cell type and diluted to 2×10^4

618 cells/ μ L. 5 μ L of cell solution was added to preformed RNP solution and gently mixed.
619 Nucleofections were performed on a Lonza HT 384-well nucleofector system using
620 program CM-120. Immediately following nucleofection, each reaction was transferred to
621 a tissue-culture treated 96-well plate containing 100 μ L normal culture media and seeded
622 at a density of 50,000 cells per well.

623 Two days post-nucleofection, DNA was extracted from using DNA QuickExtract
624 (Lucigen). Amplicons for indel analysis were generated by PCR amplification. PCR
625 products were cleaned-up and analyzed by sanger sequencing. Sanger data files and
626 sgRNA target sequences were input into Inference of CRISPR Edits (ICE) analysis
627 (ice.synthego.com) to determine editing efficiency and to quantify generated indels⁶⁵. A
628 list of all used sgRNA sequences and genotyping primers can be found in Supplementary
629 Table 4.

630

631 RT-qPCR infection assays

632 Cells were plated in 96-well plates (in triplicates for each condition) and infected the next
633 day with virus: HCoV-OC43 (moi=3), HCoV-229E (moi=0.05), SARS-CoV-2 (moi=0.01).
634 For infection with HCoVs, cells were harvested 48 hpi, lysates were reverse transcribed
635 and quantitative PCR was performed on a Bio-Rad CFX96 Touch system using the Power
636 SYBR Cells-to-CT kit (Invitrogen) according to the manufacturer's instructions. 229E and
637 OC43 RNA levels were quantified with virus-specific primer sets and viral RNA levels
638 were normalized to cellular 18S levels.

639 For SARS-CoV-2 infections, Huh7.5.1 and A549-ACE2 cells were harvested after 24 and
640 74h, respectively, using 200 μ l DNA/RNA Shield (Zymo) to inactivate virus prior to export

641 from the BSL3 laboratory. Samples were extracted using the Quick-DNA/RNA Viral
642 MagBead kit (Zymo) on a Bravo automated liquid handling platform (Agilent). Briefly, the
643 Bravo RNA extraction protocol consists of: 1) 180 µl sample transfer from 2mL deep well
644 to a 1mL deep well plate containing Proteinase K; 2) addition of Zymo Viral DNA/RNA
645 Buffer for sample lysis; 3) Addition of Zymo MagBeads; 4) 10 minute mixing and shaking
646 of samples with lysis buffer and MagBeads; 5) incubation of the mixture on a 96 well ring
647 magnet to collect the beads to a ring at the bottom of the deep well plate; 6) aspiration of
648 the supernatant and dispensing into a 2mL deep well waste plate; 7) addition of wash
649 buffers 1 with mixing; 8) incubation on the 96 well ring magnet; 9) aspiration. Steps 7-9
650 are repeated for wash buffer 2 and two rounds of 100% ethanol. 10) incubation on the
651 magnet for 20 minutes to fully evaporate residual 100% ethanol from the beads; 11)
652 Elution with nuclease-free water.

653 For RT-qPCR, separate reactions were performed for the quantification of SARS-CoV-2
654 N and E gene transcripts as well as cellular RNaseP for normalization using the Luna
655 Universal Probe One-Step RT-qPCR Kit (NEB) on a Bio-Rad CFX384 Touch system. N
656 and E gene transcripts showed high concordance and N gene levels normalized to
657 RNaseP were displayed in figures. All qPCR primer/probe sequences are listed in
658 Supplementary Table 4.

659

660 Western blots

661 Cells were lysed using Laemmli SDS sample buffer containing 5% beta-mercaptoethanol
662 and boiled at 95C for 10min. Lysates were separated by SDS-PAGE on pre-cast Bio-Rad
663 4-15% poly-acrylamide gels in Bio-Rad Mini-Protean electrophoresis system. Proteins

664 were transferred onto PVDF membranes using Bio-Rad Trans-Blot Turbo transfer
665 system. PVDF membranes were blocked with PBS buffer containing 0.1% Tween-20 and
666 5% non-fat milk. Blocked membranes were incubated with primary antibody diluted in
667 blocking buffer and incubated overnight at 4C on a shaker. Primary antibodies were
668 detected by incubating membranes with 1:5000 dilution of HRP-conjugated (Southern
669 Biotech) secondary anti-mouse and anti-rabbit antibodies for 1 h at room temperature.
670 Blots were visualized using a ChemiDoc MP Imaging System (Bio-Rad). The following
671 primary antibodies and their dilutions were used in this study: GAPDH (SCBT, sc-32233)
672 at 1:1000, ACE2 (R&D Systems, AF933) at 1:1000, TMPRSS2 (Abcam, ab92323) at
673 1:1000.

674

675 Pseudo-typed virus infection

676 Cells were plated in 96-well plates and infected with 30 µl of SARS-CoV-2 Reporter Virus
677 Particles (Integral Molecular, RVP-701) per well. After 48-72h, infection rates were
678 measured according the GFP levels using a Cytoflex flow cytometer (Beckman Coulter
679 Life Sciences).

680

681 Compounds

682 The following compounds were used in this study: SAR405 (SelleckChem, S7682),
683 YM201636 (SelleckChem, S1219), PF-429242 dihydrochloride (Sigma, SML0667) and
684 Fatostatin HBr (SelleckChem, S8284). All compounds were resuspended in DMSO and
685 stored at -20C until use.

686

687 Cell viability assay

688 Huh7.5.1 cells were treated with compounds at the same concentrations and durations
689 as in infection assays. Cell viability was measured using Cell Titer Glo (Promega)
690 according to the manufacturer's instructions.

691

692 **Supplementary Tables**

693 **Table 1:** CRISPR screen results. MaGECK output for positive gene enrichment analysis
694 of SARS-CoV-2, 229E and OC43 host factors.

695 **Table 2:** Gene ontology enrichment analysis of individual CRISPR screens and network
696 propagation clusters.

697 **Table 3:** Network propagation results.

698 **Table 4:** DNA oligo sequences used in this study.

699

700 **Data availability**

701 Raw sequencing data for CRISPR KO screens will be made available through the
702 EMBL-EBI ArrayExpress (<https://www.ebi.ac.uk/arrayexpress/>).

703

704 **Acknowledgments**

705 This research was funded by grants from the National Institutes of Health (P50AI150476,
706 U19AI135990, U19AI135972, R01AI143292, R01AI120694, P01A1063302, and
707 R01AI122747 to N.J.K.; F32CA239333 to M.B.; 5DP1DA038043 to M.O.). M.O.
708 acknowledges support through a gift from the Roddenbury. Funding to A.S.P. was
709 provided by the Chan Zuckerberg Biohub. We would like to thank Dr. Anita Sil, Dr. Bastian
710 Joehnk, Dr. Lauren Rodriguez, and Keith Walcott for BSL-3 laboratory support; Matthew
711 Laurie for help with Bravo liquid handling; Dr. Sandra Schmid, Dr. Don Ganem and Dr.
712 Françoise Chanut for editorial comments; Dr. Olga Gulyaeva, Sara Sunshine, Dr. Marco
713 Hein, Dr. Scott Biering, Dr. Nathan Meyers, and Dr. Jan Carette for helpful discussion.

714 We also express gratitude to the Biohub lab management and operations team for their
715 support.

716

717 **Author contributions**

718 R.W., C.R.S., J.K., K.T., J.M.H., J.C.S., J.O., and A.S.P. performed the experiments.

719 R.W., C.R.S., J.K. and A.S.P. designed experiments. R.W., J.K., M.B. and A.S.P.

720 analyzed and visualized data. N.J.K., M.O., K.H. and A.S.P. supervised study and

721 provided technical guidance. A.S.P. conceptualized study and wrote initial draft of the

722 manuscript. All authors provided comments and edits on the manuscript.

723

724 **Conflict of interest**

725 J.C.S., J.O. and K.H. are employees of Synthego Corporation.

726 **References**

- 727 1. van der Hoek, L. Human coronaviruses: what do they cause? *Antivir. Ther.* **12**, 651–
728 658 (2007).
- 729 2. Drosten, C. *et al.* Identification of a Novel Coronavirus in Patients with Severe Acute
730 Respiratory Syndrome. *N. Engl. J. Med.* **348**, 1967–1976 (2003).
- 731 3. Zaki, A. M., van Boheemen, S., Bestebroer, T. M., Osterhaus, A. D. M. E. &
732 Fouchier, R. A. M. Isolation of a Novel Coronavirus from a Man with Pneumonia in
733 Saudi Arabia. *N. Engl. J. Med.* **367**, 1814–1820 (2012).
- 734 4. Wu, F. *et al.* A new coronavirus associated with human respiratory disease in China.
735 *Nature* **579**, 265–269 (2020).
- 736 5. Petersen, E. *et al.* Comparing SARS-CoV-2 with SARS-CoV and influenza
737 pandemics. *Lancet Infect. Dis.* **0**, (2020).
- 738 6. Dong, E., Du, H. & Gardner, L. An interactive web-based dashboard to track COVID-
739 19 in real time. *Lancet Infect. Dis.* **20**, 533–534 (2020).
- 740 7. Fung, T. S. & Liu, D. X. Human Coronavirus: Host-Pathogen Interaction. *Annu. Rev.*
741 *Microbiol.* **73**, 529–557 (2019).
- 742 8. Letko, M., Marzi, A. & Munster, V. Functional assessment of cell entry and receptor
743 usage for SARS-CoV-2 and other lineage B betacoronaviruses. *Nat. Microbiol.* 1–8
744 (2020) doi:10.1038/s41564-020-0688-y.
- 745 9. Li, W. *et al.* Angiotensin-converting enzyme 2 is a functional receptor for the SARS
746 coronavirus. *Nature* **426**, 450–454 (2003).

- 747 10. Hofmann, H. *et al.* Human coronavirus NL63 employs the severe acute respiratory
748 syndrome coronavirus receptor for cellular entry. *Proc. Natl. Acad. Sci. U. S. A.* **102**,
749 7988–7993 (2005).
- 750 11. Hoffmann, M. *et al.* SARS-CoV-2 Cell Entry Depends on ACE2 and TMPRSS2 and
751 Is Blocked by a Clinically Proven Protease Inhibitor. *Cell* **181**, 271-280.e8 (2020).
- 752 12. Hoffmann, M., Kleine-Weber, H. & Pöhlmann, S. A Multibasic Cleavage Site in the
753 Spike Protein of SARS-CoV-2 Is Essential for Infection of Human Lung Cells. *Mol.*
754 *Cell* **78**, 779-784.e5 (2020).
- 755 13. Bertram, S. *et al.* TMPRSS2 Activates the Human Coronavirus 229E for Cathepsin-
756 Independent Host Cell Entry and Is Expressed in Viral Target Cells in the
757 Respiratory Epithelium. *J. Virol.* **87**, 6150–6160 (2013).
- 758 14. Shirato, K., Kawase, M. & Matsuyama, S. Middle East Respiratory Syndrome
759 Coronavirus Infection Mediated by the Transmembrane Serine Protease TMPRSS2.
760 *J. Virol.* **87**, 12552–12561 (2013).
- 761 15. Simmons, G. *et al.* Inhibitors of cathepsin L prevent severe acute respiratory
762 syndrome coronavirus entry. *Proc. Natl. Acad. Sci.* **102**, 11876–11881 (2005).
- 763 16. Gordon, D. E. *et al.* A SARS-CoV-2 protein interaction map reveals targets for drug
764 repurposing. *Nature* (2020) doi:10.1038/s41586-020-2286-9.
- 765 17. Stukalov, A. *et al.* Multi-level proteomics reveals host-perturbation strategies of
766 SARS-CoV-2 and SARS-CoV. *bioRxiv* 2020.06.17.156455 (2020)
767 doi:10.1101/2020.06.17.156455.
- 768 18. V'kovski, P. *et al.* Determination of host proteins composing the microenvironment of
769 coronavirus replicase complexes by proximity-labeling. *eLife* **8**, e42037 (2019).

- 770 19. Puschnik, A. S., Majzoub, K., Ooi, Y. S. & Carette, J. E. A CRISPR toolbox to study
771 virus–host interactions. *Nat. Rev. Microbiol.* **15**, 351–364 (2017).
- 772 20. Wei, J. *et al.* Genome-wide CRISPR screen reveals host genes that regulate SARS-
773 CoV-2 infection. *bioRxiv* 2020.06.16.155101 (2020)
774 doi:10.1101/2020.06.16.155101.
- 775 21. Hoffmann, H.-H. *et al.* Functional interrogation of a SARS-CoV-2 host protein
776 interactome identifies unique and shared coronavirus host factors. *bioRxiv*
777 2020.09.11.291716 (2020) doi:10.1101/2020.09.11.291716.
- 778 22. Zhu, Y. *et al.* The S1/S2 boundary of SARS-CoV-2 spike protein modulates cell
779 entry pathways and transmission. *bioRxiv* 2020.08.25.266775 (2020)
780 doi:10.1101/2020.08.25.266775.
- 781 23. Yeager, C. L. *et al.* Human aminopeptidase N is a receptor for human coronavirus
782 229E. *Nature* **357**, 420–422 (1992).
- 783 24. Ströh, L. J. & Stehle, T. Glycan Engagement by Viruses: Receptor Switches and
784 Specificity. *Annu. Rev. Virol.* **1**, 285–306 (2014).
- 785 25. Hulswit, R. J. G. *et al.* Human coronaviruses OC43 and HKU1 bind to 9-O-
786 acetylated sialic acids via a conserved receptor-binding site in spike protein domain
787 A. *Proc. Natl. Acad. Sci. U. S. A.* **116**, 2681–2690 (2019).
- 788 26. Clausen, T. M. *et al.* SARS-CoV-2 Infection Depends on Cellular Heparan Sulfate
789 and ACE2. *Cell* **0**, (2020).
- 790 27. Shisheva, A. PIKfyve and its Lipid Products in Health and in Sickness. in
791 *Phosphoinositides and Disease* (ed. FALASCA, M.) 127–162 (Springer Netherlands,
792 2012). doi:10.1007/978-94-007-5025-8_7.

- 793 28. Bilanges, B., Posor, Y. & Vanhaesebroeck, B. PI3K isoforms in cell signalling and
794 vesicle trafficking. *Nat. Rev. Mol. Cell Biol.* **20**, 515–534 (2019).
- 795 29. Brown, M. S., Radhakrishnan, A. & Goldstein, J. L. Retrospective on Cholesterol
796 Homeostasis: The Central Role of Scap. *Annu. Rev. Biochem.* **87**, 783–807 (2018).
- 797 30. Höglinger, D. *et al.* NPC1 regulates ER contacts with endocytic organelles to
798 mediate cholesterol egress. *Nat. Commun.* **10**, 4276 (2019).
- 799 31. Balderhaar, H. J. kleine & Ungermann, C. CORVET and HOPS tethering complexes
800 – coordinators of endosome and lysosome fusion. *J. Cell Sci.* **126**, 1307–1316
801 (2013).
- 802 32. Hegedüs, K. *et al.* The Ccz1-Mon1-Rab7 module and Rab5 control distinct steps of
803 autophagy. *Mol. Biol. Cell* **27**, 3132–3142 (2016).
- 804 33. Rapiteanu, R. *et al.* A Genetic Screen Identifies a Critical Role for the WDR81-
805 WDR91 Complex in the Trafficking and Degradation of Tetherin. *Traffic* **17**, 940–958
806 (2016).
- 807 34. Rong, Y. *et al.* Spinster is required for autophagic lysosome reformation and mTOR
808 reactivation following starvation. *Proc. Natl. Acad. Sci.* **108**, 7826–7831 (2011).
- 809 35. Katoh, Y. *et al.* Tollip and Tom1 Form a Complex and Recruit Ubiquitin-conjugated
810 Proteins onto Early Endosomes. *J. Biol. Chem.* **279**, 24435–24443 (2004).
- 811 36. Moretti, F. *et al.* TMEM41B is a novel regulator of autophagy and lipid mobilization.
812 *EMBO Rep.* **19**, (2018).
- 813 37. Maria Fimia, G. *et al.* Ambra1 regulates autophagy and development of the nervous
814 system. *Nature* **447**, 1121–1125 (2007).

- 815 38. Saftig, P. & Klumperman, J. Lysosome biogenesis and lysosomal membrane
816 proteins: trafficking meets function. *Nat. Rev. Mol. Cell Biol.* **10**, 623–635 (2009).
- 817 39. Flint, M. *et al.* A genome-wide CRISPR screen identifies N-acetylglucosamine-1-
818 phosphate transferase as a potential antiviral target for Ebola virus. *Nat. Commun.*
819 **10**, 285 (2019).
- 820 40. Carette, J. E. *et al.* Ebola virus entry requires the cholesterol transporter Niemann–
821 Pick C1. *Nature* **477**, 340–343 (2011).
- 822 41. Sungnak, W. *et al.* SARS-CoV-2 entry factors are highly expressed in nasal
823 epithelial cells together with innate immune genes. *Nat. Med.* **26**, 681–687 (2020).
- 824 42. Cuadrado, A. *et al.* Therapeutic targeting of the NRF2 and KEAP1 partnership in
825 chronic diseases. *Nat. Rev. Drug Discov.* **18**, 295–317 (2019).
- 826 43. Olagnier, D. *et al.* Identification of SARS-CoV2-mediated suppression of NRF2
827 signaling reveals a potent antiviral and anti-inflammatory activity of 4-octyl-itaconate
828 and dimethyl fumarate. *bioRxiv* 2020.07.16.206458 (2020)
829 doi:10.1101/2020.07.16.206458.
- 830 44. Cuadrado, A. *et al.* Can Activation of NRF2 Be a Strategy against COVID-19?
831 *Trends Pharmacol. Sci.* **41**, 598–610 (2020).
- 832 45. Maeda, Y., Ide, T., Koike, M., Uchiyama, Y. & Kinoshita, T. GPHR is a novel anion
833 channel critical for acidification and functions of the Golgi apparatus. *Nat. Cell Biol.*
834 **10**, 1135–1145 (2008).
- 835 46. Aoki, T. *et al.* Identification of the neuroblastoma-amplified gene product as a
836 component of the syntaxin 18 complex implicated in Golgi-to-endoplasmic reticulum
837 retrograde transport. *Mol. Biol. Cell* **20**, 2639–2649 (2009).

- 838 47. Mei, K. & Guo, W. The exocyst complex. *Curr. Biol.* **28**, R922–R925 (2018).
- 839 48. Lüningschrör, P. *et al.* The FTLD Risk Factor TMEM106B Regulates the Transport
840 of Lysosomes at the Axon Initial Segment of Motoneurons. *Cell Rep.* **30**, 3506-
841 3519.e6 (2020).
- 842 49. Klein, Z. A. *et al.* Loss of TMEM106B Ameliorates Lysosomal and Frontotemporal
843 Dementia-Related Phenotypes in Progranulin-Deficient Mice. *Neuron* **95**, 281-
844 296.e6 (2017).
- 845 50. Jae, L. T. *et al.* Lassa virus entry requires a trigger-induced receptor switch. *Science*
846 **344**, 1506–1510 (2014).
- 847 51. Cowen, L., Ideker, T., Raphael, B. J. & Sharan, R. Network propagation: a universal
848 amplifier of genetic associations. *Nat. Rev. Genet.* **18**, 551–562 (2017).
- 849 52. Bekerman, E. & Einav, S. Combating emerging viral threats. *Science* **348**, 282–283
850 (2015).
- 851 53. Ronan, B. *et al.* A highly potent and selective Vps34 inhibitor alters vesicle trafficking
852 and autophagy. *Nat. Chem. Biol.* **10**, 1013–1019 (2014).
- 853 54. Jefferies, H. B. J. *et al.* A selective PIKfyve inhibitor blocks PtdIns(3,5)P(2)
854 production and disrupts endomembrane transport and retroviral budding. *EMBO*
855 *Rep.* **9**, 164–170 (2008).
- 856 55. Kang, Y.-L. *et al.* Inhibition of PIKfyve kinase prevents infection by Zaire ebolavirus
857 and SARS-CoV-2. *Proc. Natl. Acad. Sci.* (2020) doi:10.1073/pnas.2007837117.
- 858 56. Ou, X. *et al.* Characterization of spike glycoprotein of SARS-CoV-2 on virus entry
859 and its immune cross-reactivity with SARS-CoV. *Nat. Commun.* **11**, 1620 (2020).

- 860 57. Bouhaddou, M. *et al.* The Global Phosphorylation Landscape of SARS-CoV-2
861 Infection. *Cell* (2020) doi:10.1016/j.cell.2020.06.034.
- 862 58. Hawkins, J. L. *et al.* Pharmacologic inhibition of site 1 protease activity inhibits sterol
863 regulatory element-binding protein processing and reduces lipogenic enzyme gene
864 expression and lipid synthesis in cultured cells and experimental animals. *J.*
865 *Pharmacol. Exp. Ther.* **326**, 801–808 (2008).
- 866 59. Kamisuki, S. *et al.* A small molecule that blocks fat synthesis by inhibiting the
867 activation of SREBP. *Chem. Biol.* **16**, 882–892 (2009).
- 868 60. Charlton, F. W. *et al.* Cellular cholesterol abundance regulates potassium
869 accumulation within endosomes and is an important determinant in bunyavirus
870 entry. *J. Biol. Chem.* **294**, 7335–7347 (2019).
- 871 61. Petersen, J. *et al.* The Major Cellular Sterol Regulatory Pathway Is Required for
872 Andes Virus Infection. *PLoS Pathog.* **10**, (2014).
- 873 62. Kleinfelter, L. M. *et al.* Haploid Genetic Screen Reveals a Profound and Direct
874 Dependence on Cholesterol for Hantavirus Membrane Fusion. *mBio* **6**, e00801
875 (2015).
- 876 63. Zang, R. *et al.* Cholesterol 25-hydroxylase suppresses SARS-CoV-2 replication by
877 blocking membrane fusion. *bioRxiv* 2020.06.08.141077 (2020)
878 doi:10.1101/2020.06.08.141077.
- 879 64. Riva, L. *et al.* Discovery of SARS-CoV-2 antiviral drugs through large-scale
880 compound repurposing. *Nature* 1–11 (2020) doi:10.1038/s41586-020-2577-1.
- 881 65. Hsiau, T. *et al.* Inference of CRISPR Edits from Sanger Trace Data. *bioRxiv* 251082
882 (2019) doi:10.1101/251082.

- 883 66. Li, W. *et al.* MAGeCK enables robust identification of essential genes from genome-
884 scale CRISPR/Cas9 knockout screens. *Genome Biol.* **15**, 554 (2014).
- 885 67. Cerami, E. G. *et al.* Pathway Commons, a web resource for biological pathway data.
886 *Nucleic Acids Res.* (2011) doi:10.1093/nar/gkq1039.
- 887 68. Su, G., Kuchinsky, A., Morris, J. H., States, D. J. & Meng, F. GLay: Community
888 structure analysis of biological networks. *Bioinformatics* (2010)
889 doi:10.1093/bioinformatics/btq596.
- 890